

ARTICLE

<https://doi.org/10.1038/s41467-019-10464-x>

OPEN

# Nickel@Siloxene catalytic nanosheets for high-performance CO<sub>2</sub> methanation

Xiaoliang Yan<sup>1,2,6</sup>, Wei Sun<sup>2,3,6</sup>, Liming Fan<sup>1</sup>, Paul N. Duchesne<sup>2</sup>, Wu Wang<sup>4</sup>, Christian Kübel<sup>4</sup>, Di Wang<sup>4</sup>, Sai Govind Hari Kumar<sup>2</sup>, Young Feng Li<sup>2</sup>, Alexandra Tavasoli<sup>2,5</sup>, Thomas E. Wood<sup>2</sup>, Darius L.H. Hung<sup>2</sup>, Lili Wan<sup>2</sup>, Lu Wang<sup>2</sup>, Rui Song<sup>2</sup>, Jiuli Guo<sup>2</sup>, Ilya Gourevich<sup>2</sup>, Abdinoor A. Jelle<sup>2</sup>, Jingjun Lu<sup>1</sup>, Ruifeng Li<sup>1</sup>, Benjamin D. Hatton<sup>5</sup> & Geoffrey A. Ozin<sup>2</sup>

Two-dimensional (2D) materials are of considerable interest for catalyzing the heterogeneous conversion of CO<sub>2</sub> to synthetic fuels. In this regard, 2D siloxene nanosheets, have escaped thorough exploration, despite being composed of earth-abundant elements. Herein we demonstrate the remarkable catalytic activity, selectivity, and stability of a nickel@siloxene nanocomposite; it is found that this promising catalytic performance is highly sensitive to the location of the nickel component, being on either the interior or the exterior of adjacent siloxene nanosheets. Control over the location of nickel is achieved by employing the terminal groups of siloxene and varying the solvent used during its nucleation and growth, which ultimately determines the distinct reaction intermediates and pathways for the catalytic CO<sub>2</sub> methanation. Significantly, a CO<sub>2</sub> methanation rate of 100 mmol<sub>g<sub>Ni</sub></sub><sup>-1</sup> h<sup>-1</sup> is achieved with over 90% selectivity when nickel resides specifically between the sheets of siloxene.

<sup>1</sup>College of Chemistry and Chemical Engineering, Taiyuan University of Technology, Taiyuan, Shanxi 030024, P. R. China. <sup>2</sup>Materials Chemistry and Nanochemistry Research Group, Solar Fuels Cluster, Department of Chemistry, University of Toronto, 80 St. George Street, Toronto, ON M5S 3H6, Canada. <sup>3</sup>State Key Laboratory of Silicon Materials and School of Materials Science and Engineering, Zhejiang University, Hangzhou, Zhejiang 310027, P. R. China. <sup>4</sup>Karlsruhe Institute of Technology (KIT), Institute of Nanotechnology (INT), Hermann-von-Helmholtz-Platz 1, Building 640, Eggenstein-Leopoldshafen 76344, Germany. <sup>5</sup>Department of Materials Science and Engineering, University of Toronto, 184 College Street, Toronto, ON M5S 3E4, Canada. <sup>6</sup>These authors contributed equally: Xiaoliang Yan and Wei Sun. Correspondence and requests for materials should be addressed to X.Y. (email: [yanxiaoliang@tyut.edu.cn](mailto:yanxiaoliang@tyut.edu.cn)) or to G.A.O. (email: [gozin@chem.utoronto.ca](mailto:gozin@chem.utoronto.ca))

Carbon dioxide (CO<sub>2</sub>) is a well-known greenhouse gas that can also be used as a zero- or even negative-cost carbon feedstock in the production of valuable chemicals and fuels<sup>1,2</sup>. This technology can be employed in the power-to-gas process, which consists of an initial hydrogen production step via electrolysis of water, followed by the reduction of CO<sub>2</sub> via the Sabatier reaction (i.e., methanation). This process of converting CO<sub>2</sub> into methane (CH<sub>4</sub>) is among the most attractive and promising technologies for transforming electrical energy into renewable chemical energy<sup>3–5</sup>. In doing so, it is possible to circumvent the considerable difficulties associated with hydrogen storage, transport, and large-scale utilization. In addition, CH<sub>4</sub> offers several benefits over hydrogen, as it is easily liquefied, can be more safely stored and transported, and is widely used in energy-intensive applications as a major component of natural gas.

For the catalysis of the CO<sub>2</sub> methanation reaction, earth-abundant and relatively low-cost Ni metal is an ideal candidate, which has led to its use being intensively explored. As the methanation reaction is highly exothermic, great effort has been devoted to anchoring or immobilizing Ni nanoparticles onto support materials in attempts to alleviate high-temperature sintering<sup>6–9</sup>. Because of such efforts, spatial confinement has emerged as an effective and unique way to limit the growth of Ni nanoparticles<sup>10,11</sup>. Chen et al.<sup>11</sup> pointed out that a “cage” of mesoporous SBA-16 could confine small Ni nanoparticles, thereby contributing to their high activity in the reverse water–gas shift reaction (i.e., hydrogenation of CO<sub>2</sub> to CO). However, the design and fabrication of Ni catalysts with high selectivity toward CH<sub>4</sub> production, rather than the competing reverse water–gas shift reaction, remains a major challenge. In addition, the reaction mechanism for Ni catalysts is still largely ambiguous, both under laboratory conditions and in industrial applications.

Only recently have theoretical and modeling studies begun to show some evidence regarding the CO<sub>2</sub> methanation mechanism<sup>12–14</sup>. Heine et al.<sup>14</sup> used ambient-pressure X-ray photoelectron spectroscopy (XPS) to probe the reaction pathways for CO<sub>2</sub> methanation on a Ni (111) surface. In this system, CO<sub>2</sub> first dissociated to CO and atomic oxygen at the Ni surface, whereupon CO then decomposed to atomic carbon (\*C) before finally being converted to CH<sub>4</sub> via hydrogenation. This reaction pathway inevitably yields significant quantities of CO and may lead to catalyst poisoning via carbonization (coking) of the catalyst surface.

In this context, a superior Ni catalyst must have high activity and selectivity toward CH<sub>4</sub> production, as well as good stability under operating conditions. A unique pathway for sustainable CH<sub>4</sub> production must therefore be achieved by designing the chemistry and structure of not only Ni itself but, more importantly, the supporting materials used to accomplish the desired surface engineering and spatial confinement.

Silicon, being the second most earth-abundant element, is clearly deserving of investigation for such use. Aside from mesoporous silica, which could supply the aforementioned two-dimensional (2D) or three-dimensional (3D) confinement effect<sup>15–17</sup>, and some reports on metal on porous Si<sup>18–21</sup>, the most widely used form of Si for supporting catalysts is SiO<sub>2</sub> particles, without further chemical or structural design. SiO<sub>2</sub>-supported Ni catalysts have relatively low selectivity toward CH<sub>4</sub> production (lower than 80%) with the remaining ca. 20% selectivity being toward CO<sup>22</sup>. In this regard, various promoters were added to improve the CH<sub>4</sub> production selectivity of the Ni/SiO<sub>2</sub> catalysts<sup>23–25</sup>. In addition, production selectivity could be switched from CO to CH<sub>4</sub> on Ni/SiO<sub>2</sub> catalysts by increasing the Ni loading from 0.5 wt% to a much higher value of 10 wt%<sup>26</sup>.

However, it is still a challenge to design silicon-supported Ni catalysts with a distinctive structure and superior selectivity for CO<sub>2</sub> methanation. In an era where 2D catalyst materials are both in great demand and showing significant promise scientifically and technologically, 2D silicon nanosheet materials have historically been overlooked. Only a few reports for its use in catalysis can be found, exemplifying its use in water splitting<sup>27</sup>, ethylene polymerization<sup>28</sup>, formic acid decomposition<sup>29</sup>, 4-nitrophenol reduction<sup>30</sup>, and butene isomerization<sup>31</sup>. In this report, we employ 2D silicon surface chemistry to design catalysts consisting of Ni on siloxene nanosheets (SiXNS), in order to address the challenges posed by CO<sub>2</sub> methanation. Hydride- and hydroxyl-terminated layered silicon was chosen as the starting material for designing and constructing the uniquely supported Ni nanostructures used in this study. It is shown herein that Si–H hydrolysis can be triggered or avoided during synthesis by using a water- or ethanol-based Ni<sup>2+</sup> precursor solution, respectively. This strategic choice also determines whether Ni nanoparticles are obtained on the interior or exterior of the SiXNS. The Ni nanoparticles confined inside the SiXNS exhibit improved catalytic activity and selectivity to CH<sub>4</sub> relative to those on the surface of SiXNS, and this catalytic performance can be further improved under photothermal reaction conditions. With evidence from in-situ infrared studies, two distinct pathways for CO<sub>2</sub> methanation are observed for these two classes of materials, providing the insight and designing strategy for composite catalysts and materials with structural confinement effects.

## Results

**Materials design and fabrication process.** SiXNS were exfoliated from bulk calcium silicide at 0 °C using concentrated HCl<sup>27,32,33</sup>. The composition and structure of such exfoliated 2D nanosheets have been studied for decades. Three main types of structures containing Si–H and different types of O sites have been proposed: first, the Weiss siloxene consisting of corrugated Si (111) layers terminated above and below by OH and H groups<sup>34</sup>; second, the Kautsky siloxene consisting of puckered Si six rings interconnected by oxygen bridges<sup>35</sup>; and third, an unusual structure wherein linear Si chains are interconnected via oxygen bridges and terminated by hydrogen<sup>27</sup>. When actually synthesized in the lab, a mixture of the above mentioned structures with the general formula of Si<sub>6</sub>O<sub>x</sub>(OH)<sub>y</sub>H<sub>6–y</sub> is observed, in which Si is terminated by –H and –OH functional groups, with Si–O–Si bridges also existing<sup>36,37</sup>. Such configurations allow for dispersion in common polar solvents, such as water and ethanol, facilitating the next step of nanocomposite formation using the soluble Ni salt. A dispersion of the fresh SiXNS was mixed and sonicated with a nickel nitrate solution, dried by heating under vacuum, and then calcined under air at 400 °C for 3 h. This procedure resembles the widely used impregnation method for producing conventional supported metal catalysts; however, it was found that the choice of solvent (i.e., water or ethanol), resulted in different structures in the product material. Figure 1a illustrates the philosophy of the design strategy: the circle of Taiji represents the unity of beginning from the same precursor, whereas the separated black and white halves symbolize the difference of the final products. When using water as the solvent, both the hydrolysis of the Si–H perpendicular to the plane to form Si–OH and the condensation of Si–OH into Si–O–Si will proceed during the impregnation process, as was also observed by Weiss et al.<sup>34</sup> (the pioneer of the siloxene material) and, more recently, by Xie et al.<sup>27</sup>. This hydrolysis by water appears to inhibit the infiltration and deposition of nickel nitrate between the siloxene sheets. In contrast, ethanol preserves more Si–H and results in less condensation of Si–OH. These mechanisms are evidenced by

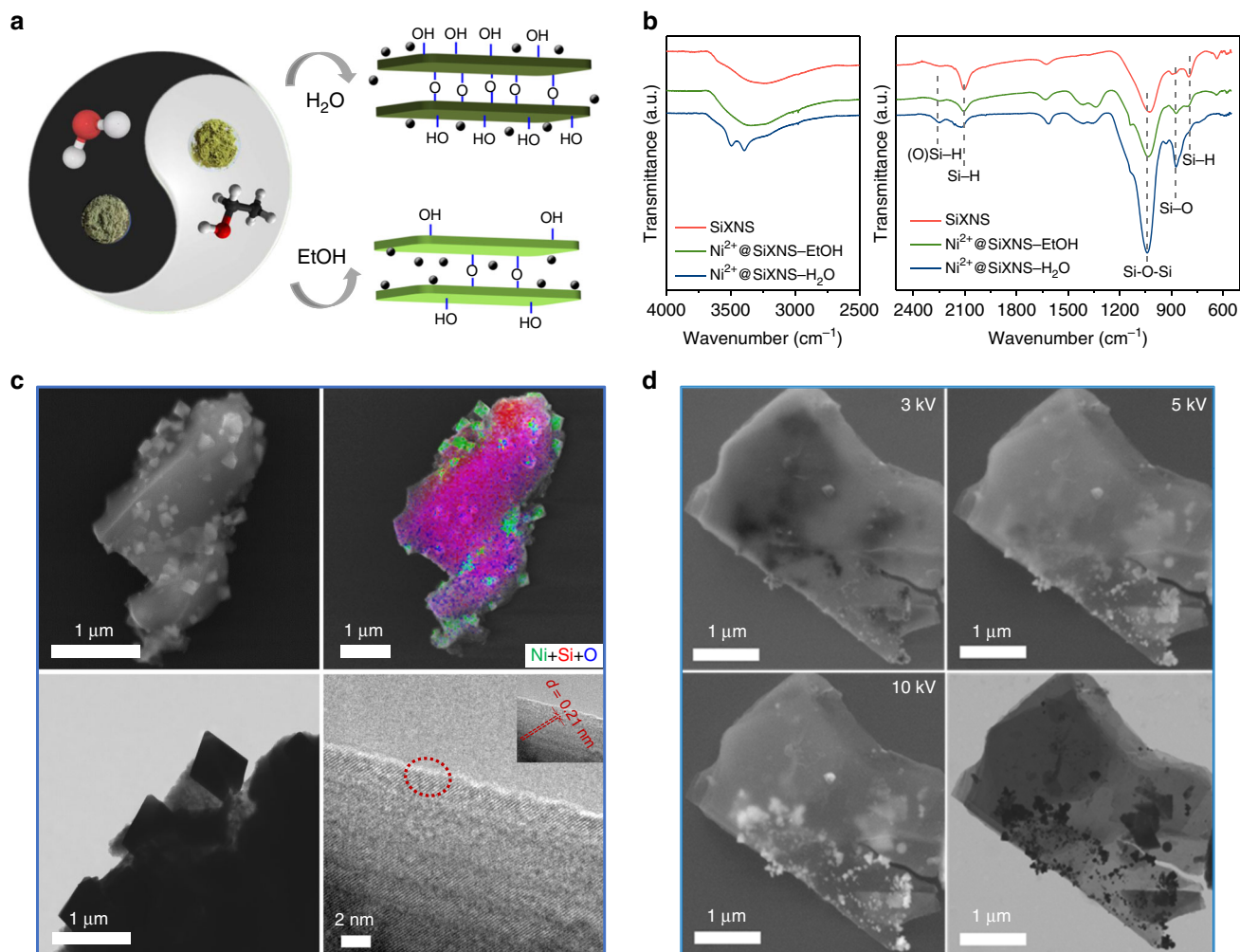


**Fig. 1** Preparation, growth, and electron microscopy characterization of NiO@SiXNS. **a** Structures of two different Ni<sup>2+</sup>-impregnated SiXNS samples. The taijitu symbolizes the fact that, when used as the solvent, H<sub>2</sub>O and EtOH, result in two distinct composite structures, despite being derived from the same solid siloxene precursor. The black spheres around the green SiXNS slabs indicate the Ni<sup>2+</sup> ions. **b** FTIR spectra of pristine SiXNS and SiXNS impregnated with Ni<sup>2+</sup> ions in EtOH and H<sub>2</sub>O. **c** Scanning electron microscopy (SEM) with energy-dispersive X-ray (EDX) and transmission electron microscopy (TEM) images of NiO@SiXNS-H<sub>2</sub>O, and **d** SEM and TEM images of NiO@SiXNS-EtOH

Fourier-transform infrared (FTIR) spectroscopy (Fig. 1b) of samples prepared using either water or ethanol. The spectrum of the SiXNS impregnated in ethanol resembles that of the original pristine SiXNS, with the extra peaks at around 1350 cm<sup>-1</sup> assigned to nitrate ions. In contrast, the sample impregnated in water exhibits significantly increased Si-O-Si peaks due to condensation of Si-OH, a weak mode at around 2100 cm<sup>-1</sup> for Si-H, and distinctive Si-OH modes between 3250 and 3500 cm<sup>-1</sup>, due to more extensive hydrolysis of Si-H. As a result, following the decomposition of nickel nitrate via calcination, the NiO so produced tended to be located on the more extensively hydrolyzed exterior surface of the stacked SiXNS impregnated in water (NiO@SiXNS-H<sub>2</sub>O) but between the sheets of less-hydrolyzed SiXNS impregnated in ethanol (NiO@SiXNS-EtOH). Due to this unique siloxene chemistry, significantly different final structures were obtained from the same precursor material. Notably, the Ni loadings were almost the same for NiO@SiXNS-H<sub>2</sub>O and NiO@SiXNS-EtOH, (4.9 and 4.7 wt%, respectively), as determined using inductively coupled-plasma atomic emission spectroscopy (ICP-AES).

The morphology and microstructure of fresh NiO@SiXNS was examined using electron microscopy; representative images are shown in Fig. 1c, d. Scanning electron microscopy (SEM) and

transmission electron microscopy (TEM) images of NiO@SiXNS-H<sub>2</sub>O showed that NiO nanoparticles were deposited on the external surface of SiXNS. This can be further illustrated by the patterns of green (Ni) octahedra scattered across the red (Si) support, whereas the blue (O) component is more homogeneously distributed throughout the material, as obtained from energy-dispersive X-ray (EDX) mapping analysis (Fig. 1c). The lattice fringe of 0.21 nm on NiO@SiXNS-H<sub>2</sub>O originates from the NiO (200) plane, further confirming the identity of the phase. In contrast, NiO nanoparticles formed on NiO@SiXNS-EtOH grew between the sheets of SiXNS. In the SEM images shown in Fig. 1d, very few particles could be observed on the exterior surface. Only by increasing the accelerating voltage could more and brighter particles be revealed, exhibiting distinctive contrast against the surrounding SiXNS as the penetration ability of the accelerated electrons increased. Providing crucial support for this observation is the fact that TEM imaging clearly revealed the majority of NiO particles were encapsulated within the SiXNS and could not be observed using low-voltage SEM.

**Characterization of NiO@SiXNS materials.** Powder X-ray diffraction (PXRD) (Fig. 2a) studies of the NiO@SiXNS-H<sub>2</sub>O and

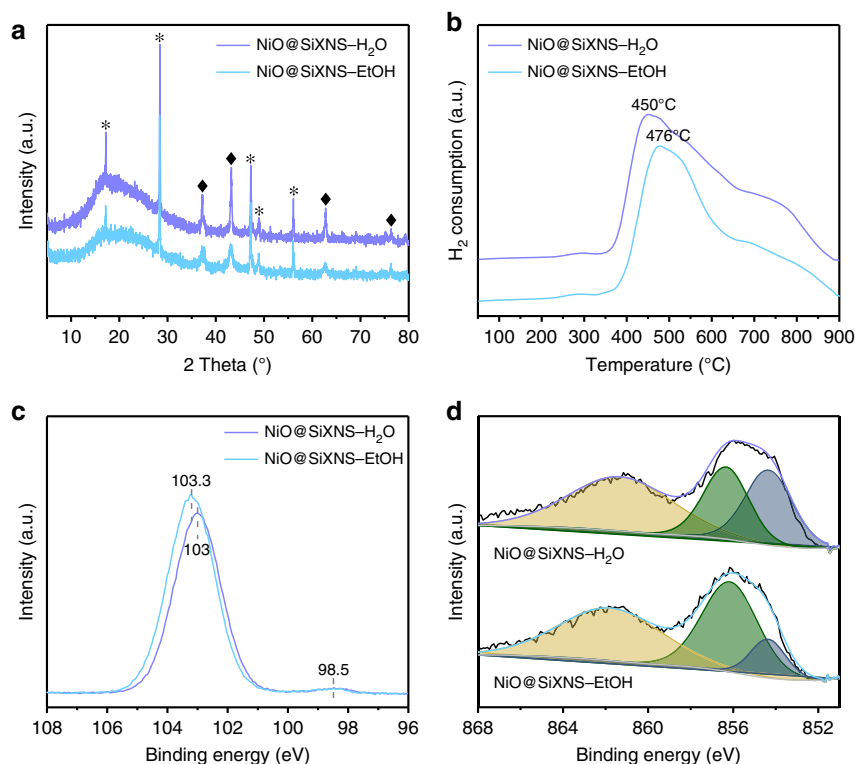


**Fig. 2** Characterization of NiO@SiXNS materials. **a** PXRD patterns showing characteristic peaks from the (\*) SiXNS and (◆) NiO constituents of the composite materials. **b** H<sub>2</sub>-TPR (hydrogen temperature programmed reduction) plots indicating the appreciable difference in the onset of NiO reduction on heating under a hydrogen atmosphere. **c, d** XPS spectra illustrating the differences in the local bonding environments of **c** Si 2*p* and **d** Ni 2*p*<sub>3/2</sub> obtained from NiO@SiXNS samples (green peak refers to NiSiO<sub>3</sub>, cyan peak corresponds to NiO, and yellow one is the satellite peak)

NiO@SiXNS-EtOH were carried out in order to better understand their structure. In addition to the peaks associated with SiXNS exfoliated from CaSi<sub>2</sub> (marked with asterisks)<sup>37</sup>, both samples exhibited one broad peak at ~20° (corresponding to the presence of an amorphous phase) and four obvious peaks (marked with rhombuses) corresponding to NiO. The slightly broader peaks of NiO in NiO@SiXNS-EtOH also implies that spatial confinement limits the nucleation and growth process. The Brunauer–Emmett–Teller (BET) surface areas of NiO@SiXNS-H<sub>2</sub>O and NiO@SiXNS-EtOH are 8.8 and 9.1 m<sup>2</sup> g<sup>-1</sup>, respectively (Supplementary Fig. 1).

The reduction properties of NiO@SiXNS was measured by using hydrogen temperature programmed reduction (Fig. 2b). Slight hydrogen consumption begins at 250 °C for both samples. A major peak was observed at 450 °C for NiO@SiXNS-H<sub>2</sub>O, whereas the corresponding peak was not observed until 476 °C for NiO@SiXNS-EtOH, which also exhibited a shoulder peak at ~700 °C. The major peak in these TPR profiles originates from the reduction of NiO. The higher reduction temperature of NiO@SiXNS-EtOH relative to NiO@SiXNS-H<sub>2</sub>O is attributed to the fact that, in the former case, NiO nanoparticles are trapped inside the SiXNS and well-anchored to the support, whereas, in the latter, NiO nanoparticles are mainly located on the exterior where they are more exposed to the hydrogen reductant. The small peak at ~700 °C on the TPR profiles of NiO@SiXNS is attributed to the presence of silicate species<sup>38</sup>.

XPS spectroscopy (Fig. 2c, d) revealed more detailed information about NiO@SiXNS. The Si 2*p* spectra showed key peaks at the binding energies of 98.5 and 103 eV, corresponding to siloxene Si<sup>0</sup> and Si<sup>4+</sup> sites, respectively. The predominance of Si<sup>4+</sup> compared with Si<sup>0</sup> can be attributed to oxidation during the calcination process. In addition, spectra from both samples exhibited broad, asymmetric peaks in the Ni 2*p*<sub>3/2</sub> region. This

region consisted of two peaks at binding energies of 854.5 and 856.3 eV, which represent NiO and a nickel silicate (NiSiO<sub>3</sub>) phase, respectively<sup>39</sup>. According to the deconvoluted XPS results, the NiSiO<sub>3</sub>-to-NiO peak area ratio of NiO@SiXNS-EtOH (3.6) was four times of that for NiO@SiXNS-H<sub>2</sub>O (0.9). This difference further supports the preferred location of NiO at interior sites in NiO@SiXNS-EtOH, as more NiO should be sandwiched between SiXNS.

**Characterization of Ni@SiXNS materials.** In order to determine the structure of the catalysts, the reduced Ni@SiXNS were further characterized. Accurate 3D visualization of the confined architecture of Ni@SiXNS-EtOH was achieved via electron tomography analysis (Fig. 3 and Supplementary Movie 1). The majority of the nanoparticles are seemingly encapsulated within the interlayer spaces of adjacent nanosheets (Fig. 3a and Supplementary Movie 1). Almost no nanoparticles were observed on the top and bottom of the nanosheets (Fig. 3b, e); in contrast, most of the nanoparticles with bright contrast were revealed in slices deeper within the 3D reconstruction of this composite particulate (Fig. 3c, d).

The PXRD patterns of Ni@SiXNS catalysts revealed that both Ni and NiO were present following reduction (Fig. 4a, b). TEM images of the Ni@SiXNS-H<sub>2</sub>O and Ni@SiXNS-EtOH, shown in Fig. 4c and Supplementary Fig. 2, further revealed that Ni nanoparticles were exposed on the exterior of the SiXNS, and that well-defined lattice fringes of 0.176 and 0.21 nm associated with Ni (200) and NiO (200) planes are observed on Ni@SiXNS-H<sub>2</sub>O. On Ni@SiXNS-EtOH, the majority of Ni nanoparticles are sandwiched between SiXNS sheets and only a few Ni nanoparticles are immobilized on the outer surface as seen in the thinner regions of SiXNS (Supplementary Fig. 3). The lattice fringes of 0.176 nm and 0.210 nm can also be ascribed to Ni (200) and NiO



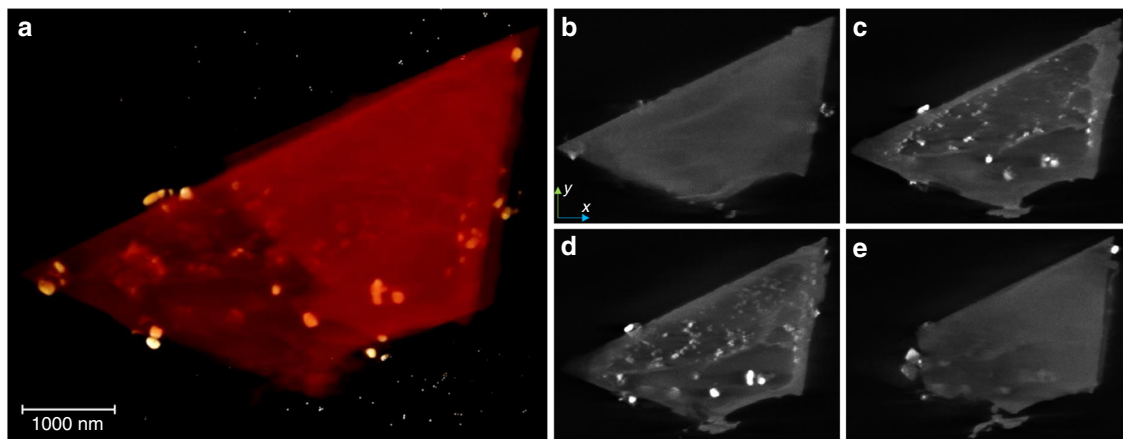


**Fig. 3** Electron tomography analysis of Ni@SiXNS-EtOH. **a** A screenshot image depicting the volume rendering of the 3D reconstruction and **b-e** images of slices obtained at different *z* depths of the 3D reconstruction of a particulate of Ni@SiXNS-EtOH. Slices shown in **b** and **e** reveal almost no Ni-containing nanoparticles on the top and bottom of the composite particulate, whereas those shown in **c**, **d** reveal the presence of Ni-containing nanoparticles in the interlayer spaces between SiXNS. Tiny, scattered white dots in the background of **a** are the added gold nanoparticles as track markers

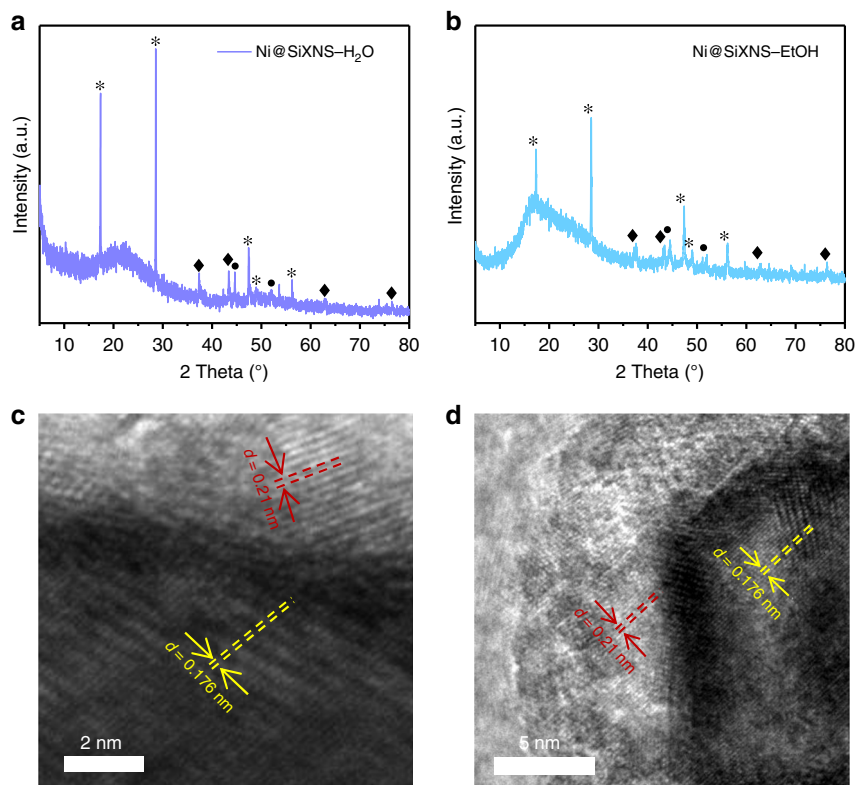


**Fig. 4** Characterization of Ni@SiXNS Materials. **a**, **b** PXRD patterns showing characteristic peaks from the (●) Ni, (◆) NiO, and (\*) SiXNS constituents of **a** Ni@SiXNS-H<sub>2</sub>O and **b** Ni@SiXNS-EtOH. **c**, **d** TEM images of **c** Ni@SiXNS-H<sub>2</sub>O and **d** Ni@SiXNS-EtOH

(200) planes, respectively (Fig. 4d). The Ni surface area and size of Ni@SiXNS were determined using H<sub>2</sub> chemisorption measurements. Similar Ni surface areas of 3.8 and 4.0 m<sup>2</sup> g<sub>cat</sub><sup>-1</sup> were observed for the Ni@SiXNS-H<sub>2</sub>O and Ni@SiXNS-EtOH, respectively. The sizes of Ni particles were also similar, being 10.7 nm for Ni@SiXNS-H<sub>2</sub>O and 10.3 nm for Ni@SiXNS-EtOH. These resemblances suggest that the surface area and size of Ni in these catalysts are not responsible for the observed differences in their catalytic performance.

**Catalytic performance of CO<sub>2</sub> methanation.** The catalytic activity of the Ni@SiXNS catalysts for the CO<sub>2</sub> methanation was

tested at 300 °C in a flow reactor system operating at atmospheric pressure under a flowing H<sub>2</sub>/CO<sub>2</sub> atmosphere (4:1). The pristine SiXNS (calcined at 400 °C for 3 h) showed no activity toward CO<sub>2</sub> methanation either in the dark or light under the same reaction conditions. For the composite catalyst materials, however, significant activity was observed, with CH<sub>4</sub> and CO being identified as the only products generated by these Ni@SiXNS catalysts under both dark and light conditions (Fig. 5). The CH<sub>4</sub> and CO production rates for Ni@SiXNS-H<sub>2</sub>O in the dark were found to be 36.6 and 32.0 mmol g<sub>Ni</sub><sup>-1</sup> h<sup>-1</sup>, respectively, which increased to 41.0 and 34.5 mmol g<sub>Ni</sub><sup>-1</sup> h<sup>-1</sup> on exposure to light (Fig. 5a, b). Despite this rate increase, CH<sub>4</sub> selectivity remained virtually

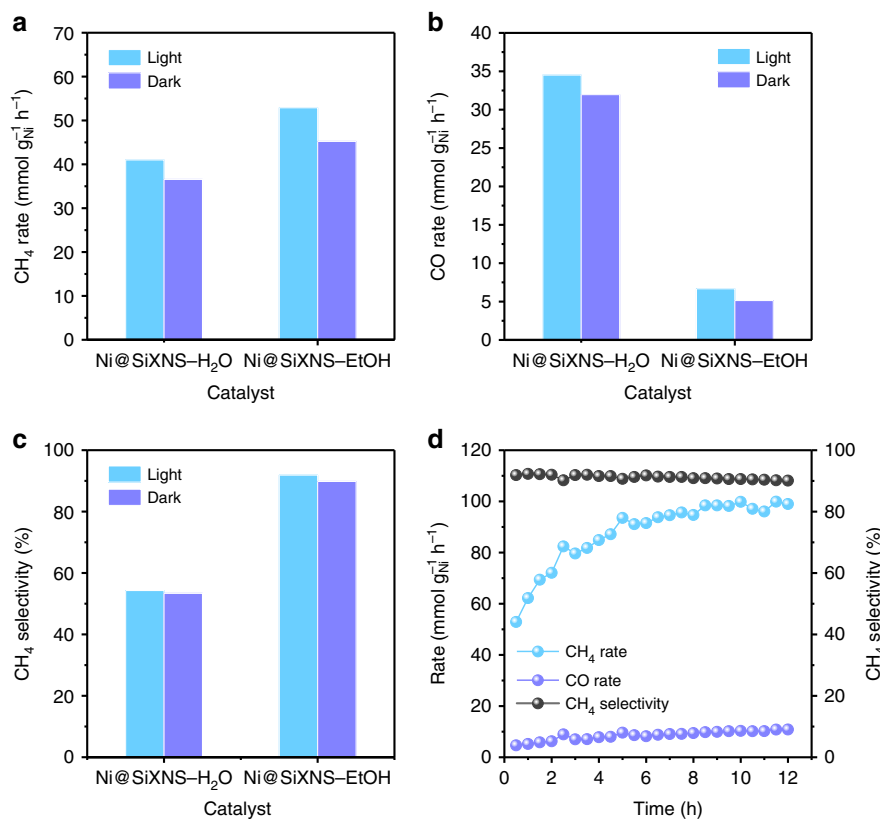


**Fig. 5** Catalytic performance of CO<sub>2</sub> methanation on Ni@SiXNS. **a**, **b** Observed catalytic rates for **a** CH<sub>4</sub> production and **b** CO production by Ni@SiXNS samples under light and dark conditions. **c** CH<sub>4</sub> selectivity of Ni@SiXNS samples for CO<sub>2</sub> methanation under light and dark conditions. **d** CH<sub>4</sub> production rate and selectivity as well as CO production rate of Ni@SiXNS-EtOH for CO<sub>2</sub> methanation under illumination for a continuous 12 h at atmospheric pressure

unchanged, with calculated values of 53.4% and 54.3% upon switching from dark to light operating conditions (Fig. 5c). This slightly enhanced performance is attributed to the photothermal effect of the Ni particles in Ni@SiXNS-H<sub>2</sub>O. The diffuse reflectance spectrum of the sample is low throughout the visible spectral region because of the significant visible light-harvesting capacity (interband and intraband electronic transitions) of the black Ni nanoparticles, which should favor local heating of Ni via the photothermal effect (Supplementary Fig. 4)<sup>40</sup>.

As a control experiment, commercial amorphous silicon dioxide-supported nickel (Ni@SiO<sub>2</sub>) was employed and loaded into the same flow catalyst reactor for evaluation under the same conditions. The Ni loading and mass of the Ni@SiO<sub>2</sub> used were the same as those of Ni@SiXNS. As shown in Supplementary Fig. 5, the CH<sub>4</sub> and CO production rates in the dark over Ni@SiO<sub>2</sub> are 22.78 and 193.70 mmol g<sub>Ni</sub><sup>-1</sup> h<sup>-1</sup>, respectively. In this case, CH<sub>4</sub> selectivity is only 10.5%, significantly lower than that of Ni@SiXNS-H<sub>2</sub>O. Under light conditions, CH<sub>4</sub> and CO production rates increase to 34.55 and 296.09 mmol g<sub>Ni</sub><sup>-1</sup> h<sup>-1</sup>, whereas CH<sub>4</sub> selectivity still remains at 10.5%. The result indicates that Ni supported on SiO<sub>2</sub> favors the reverse water-gas shift reaction, contributing to the formation of large amount of CO rather than CH<sub>4</sub>. We attribute the lower selectivity toward CH<sub>4</sub> to the poorer contact between Ni and commercial spherically shaped SiO<sub>2</sub> particles compared with that between the Ni and the planar SiXNS.

In an attempt to improve the selectivity toward the production of CH<sub>4</sub>, Ni@SiXNS-EtOH with Ni nanoparticles trapped between the sheets was also tested for its CO<sub>2</sub> methanation activity, as shown in Fig. 5. Notably, CH<sub>4</sub> and CO production rates for this

catalyst increased from 45.2 and 5.1 mmol g<sub>Ni</sub><sup>-1</sup> h<sup>-1</sup>, respectively, in the dark to 52.9 and 6.7 mmol g<sub>Ni</sub><sup>-1</sup> h<sup>-1</sup> in the light (Fig. 5a, b). The CH<sub>4</sub> selectivity increased slightly from 89.8% in the dark to 91.9% in the light (Fig. 5c). Isotopic labeling experiments using <sup>13</sup>C and gas chromatography-mass spectrometry (GC-MS) were used to study the products generated from a <sup>13</sup>CO<sub>2</sub> reactant feed. The mass-to-charge (*m/z*) ratios observed at 17 and 29 amu in the GC-MS spectrum corresponded to <sup>13</sup>CH<sub>4</sub> and <sup>13</sup>CO (Supplementary Fig. 6), confirming that CH<sub>4</sub> and CO are, indeed, produced from the methanation of CO<sub>2</sub> on Ni@SiXNS and not from adventitious carbon contaminants. Thus, Ni@SiXNS-EtOH exhibited both higher selectivity and activity for the CO<sub>2</sub> methanation than Ni@SiXNS-H<sub>2</sub>O.

The catalytic stability at 300 °C with light of Ni@SiXNS-EtOH was next investigated, as illustrated in Fig. 5d. The CH<sub>4</sub> production rate increased progressively and reached a stable value around an impressive 100 mmol g<sub>Ni</sub><sup>-1</sup> h<sup>-1</sup> during the 12 h test, whereas the CO production rate increased only slightly and stabilized around 10 mmol g<sub>Ni</sub><sup>-1</sup> h<sup>-1</sup>. In addition, CH<sub>4</sub> selectivity was observed to remain stable at above ~90%. One can therefore deduce that Ni@SiXNS-EtOH is a highly active, selective, and stable catalyst for the preferential hydrogenation of CO<sub>2</sub> to CH<sub>4</sub>. The catalytic performance of an industrial Ni@Al<sub>2</sub>O<sub>3</sub> catalyst is shown as a reference for comparison in Supplementary Fig. 7. CH<sub>4</sub> and CO production rates in the light over Ni@Al<sub>2</sub>O<sub>3</sub> are 28.69 and 0.63 mmol g<sub>Ni</sub><sup>-1</sup> h<sup>-1</sup> with a CH<sub>4</sub> selectivity of 97.8% in the first 30 min and slightly decreased and maintained at 27.78 and 0.55 mmol g<sub>Ni</sub><sup>-1</sup> h<sup>-1</sup> with similar selectivity. Although Ni@Al<sub>2</sub>O<sub>3</sub> has higher CH<sub>4</sub> selectivity than that of Ni@SiXNS-EtOH, the production rates are much lower.

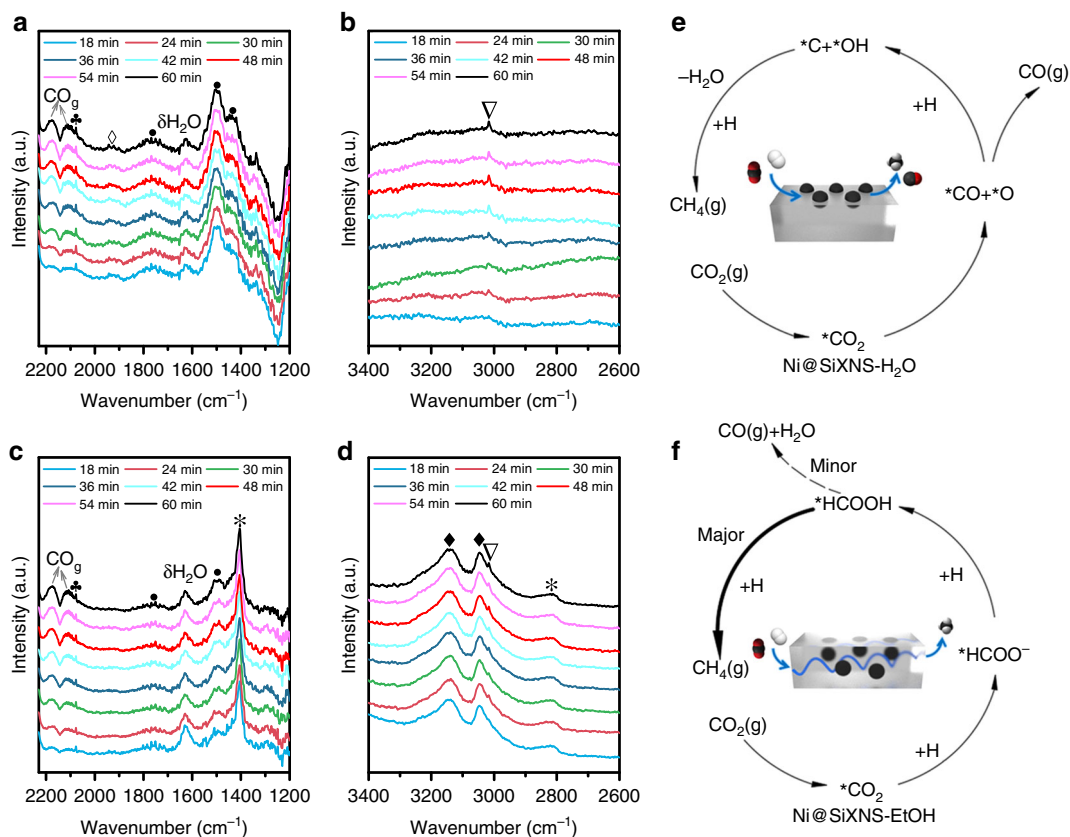


**Fig. 6** In-situ DRIFTS experiments and proposed catalytic pathways. **a–d** In-situ DRIFTS spectra of samples Ni@SiXNS-H<sub>2</sub>O (**a, b**) and Ni@SiXNS-EtOH (**c, d**). **e, f** The catalytic reaction pathways of Ni@SiXNS-H<sub>2</sub>O- (**e**) and Ni@SiXNS-EtOH- (**f**) catalyzed CO<sub>2</sub> reduction and the key reactions involved that can be detected by DRIFTS. Symbols: (●) linear CO; (◊) bridging CO; (●) carbonate; (▽) CH<sub>4</sub>; (\*) formate; (◆) OH groups

**Catalytic reaction pathways.** To gain deeper insights into the CO<sub>2</sub> methanation reaction over Ni@SiXNS, in-situ diffuse reflectance infrared Fourier transform spectroscopy (DRIFTS) studies were conducted. Each NiO@SiXNS sample was reduced in the DRIFTS sample cell for 1 h under a H<sub>2</sub> atmosphere and then purged for 1 h under He at 300 °C. Next, the sample was exposed to a mixture of CO<sub>2</sub> (2 s.c.c.m.), H<sub>2</sub> (8 s.c.c.m.), and He (10 s.c.c.m.) for 1 h. We focused our analysis on the IR fingerprint regions of 1200–2200 cm<sup>-1</sup> and 2600–3400 cm<sup>-1</sup> in the consecutive spectra, where reaction intermediates could be detected.

For Ni@SiXNS-H<sub>2</sub>O, two key reaction intermediates were observed, as shown in Fig. 6a. The first, identified as chemisorbed CO<sub>2</sub> had observable peaks at 1430 and 1500/1767 cm<sup>-1</sup>, and is diagnostic of the formation of bicarbonate and carbonate species, respectively<sup>41–44</sup>. The second was identified from peaks located at 1930 and 2077 cm<sup>-1</sup>, which are attributed to the presence of bridging and linearly adsorbed CO molecules on Ni, respectively<sup>45,46</sup>. As depicted in Fig. 6b, C–H stretching vibrations of CH<sub>4</sub> were also detected at 3016 cm<sup>-1</sup>, with additional peaks at 2111/2174 and 1630 cm<sup>-1</sup> being observed for gaseous CO and H<sub>2</sub>O, respectively<sup>6</sup>.

For Ni@SiXNS-EtOH, apart from the carbonate species, one important reaction intermediate appeared at 1404 cm<sup>-1</sup> in the spectra (Fig. 6c) and was ascribed to a surface formate species (HCO<sub>2</sub><sup>-</sup>)<sup>47,48</sup>; this assignment is supported by an additional peak observed at 2814 cm<sup>-1</sup> (Fig. 6d)<sup>11,49</sup>. It is noteworthy that the peak intensity of this formate species is much higher than that of the carbonate species. Yet, another species with corresponding peaks at 3046 and 3140 cm<sup>-1</sup> matched well with those of hydroxyl groups, as reported in the literature<sup>50</sup>. It should be

noted that no obvious peaks could be detected in the range of 2000–1800 cm<sup>-1</sup> for Ni@SiXNS-EtOH, which reveals the essential absence of bridging CO; this is likely because Ni nanoparticles in the catalyst are trapped between sheets of SiXNS, thus decreasing the chance for the bonding of CO molecules to multiple Ni atoms. Only gaseous CO appears in the spectra, as well as gaseous CH<sub>4</sub> and H<sub>2</sub>O.

Based on the differential DRIFTS spectra of the Ni@SiXNS catalysts, a reaction pathway for CO<sub>2</sub> methanation was proposed (Fig. 6e, f). As the Ni nanoparticles were located on the exterior surface of SiXNS in Ni@SiXNS-H<sub>2</sub>O, these particles are readily exposed to CO<sub>2</sub>, whereupon the chemisorbed \*CO<sub>2</sub> species can dissociate into \*CO and \*O. The strongly bound, bridge-bonded \*CO species indicated by the IR data can further dissociate to carbon species (\*C), which can then be hydrogenated to form CH<sub>4</sub> and desorb from the catalyst surface, corresponding to the observed CH<sub>4</sub> production, whereas the \*O species can react with hydrogen to produce H<sub>2</sub>O. However, the stable bridging \*CO species also have a higher chance to convert to CO as the final product, leading to an overall lower selectivity to CH<sub>4</sub>.

In contrast, Ni nanoparticles in Ni@SiXNS-EtOH are confined within SiXNS and the bridging \*CO species cannot be readily formed. A recent theoretical calculation has shown that a silica-cluster-modified Ni (111) surface has a higher activation energy barrier for the dissociation of \*CO<sub>2</sub> to CO through the \*CO pathway than a clean exposed Ni (111) surface<sup>51</sup>. Our DRIFTS spectra and catalytic performance tests on Ni@SiXNS-EtOH are consistent with the prediction that the generation of \*CO, and thus CO, is limited due to the Ni nanoparticles being encased within the SiXNS. Therefore, the chemisorbed \*CO<sub>2</sub> species for

this structure could instead convert first to  $\text{HCO}_2^-$  and then to formic acid ( $\text{HCOOH}$ ). More pronounced C–H IR mode intensity from  $\text{HCOOH}$  could be detected by quickly cooling down the reactor during DRIFTS measurements (Supplementary Fig. 8)<sup>49</sup>. A small portion of the  $\text{HCOOH}$  so generated could decompose to gaseous  $\text{CO}$  and  $\text{H}_2\text{O}$ ; however, a larger proportion is likely to participate in the rapid generation of  $\text{CH}_4$ , possibly by the formate pathway reported by Kattel et al.<sup>52</sup>. This additional pathway for  $\text{CH}_4$  production on  $\text{Ni@SiXNS-EtOH}$  could be due to the tortuosity experienced by  $\text{CO}_2$  within the interior of the catalyst, which enhances the probability of it being fully hydrogenated to  $\text{CH}_4$  via the associative  $\text{CO}_2$  methanation mechanism (in which carbonate is hydrogenated to bicarbonate and then quickly dehydrated to formate)<sup>53</sup>. Besides, the newly generated OH groups observed in Fig. 6d could provide additional H source and aid in formate formation<sup>47</sup>.

## Discussion

The synthesis of  $\text{Ni@SiXNS}$  nanocomposites relies on a distinctive kind of silicon surface chemistry in which the Si–H hydrolysis and Si–OH condensation are selectively triggered or avoided. The resulting  $\text{Ni@SiXNS}$  materials are extremely active toward the conversion of  $\text{CO}_2$  to  $\text{CH}_4$  with high selectivity and impressive stability. The nucleation and growth of Ni nanoparticles on either the exterior or interior of the SiXNS was solvent-sensitive, enabled by choosing water or ethanol, respectively. After a standard impregnation–calcination–reduction in water, a  $\text{Ni@SiXNS-H}_2\text{O}$  catalyst was produced. For this material, Ni nanoparticles were immobilized on the exterior surface of the SiXNS. The corresponding  $\text{CH}_4$  production rate was  $41.0 \text{ mmol g}_{\text{Ni}}^{-1} \text{ h}^{-1}$  with heating at  $300^\circ\text{C}$  with assistance of light, but  $\text{CH}_4$  selectivity was only 54.3%. In contrast, the  $\text{Ni@SiXNS-EtOH}$  catalyst favored Ni located within the interlayer space of the SiXNS. These samples featured a  $\text{CH}_4$  production rate of  $52.9 \text{ mmol g}_{\text{Ni}}^{-1} \text{ h}^{-1}$  and a  $\text{CH}_4$  selectivity over 90%. This spatially confined Ni catalyst proved stable in the light and, over time, eventually reaching an impressive  $\text{CH}_4$  production rate of  $\sim 100 \text{ mmol g}_{\text{Ni}}^{-1} \text{ h}^{-1}$  with  $\sim 90\%$  selectivity.

An in-situ infrared study clarified the reaction pathways of the  $\text{Ni@SiXNS}$  catalysts for  $\text{CO}_2$  methanation, revealing the origin of the observed differences in selectivity between the two types of structures. Distinct reaction intermediates (i.e.,  $\text{CO}$  and formate species) were observed on the  $\text{Ni@SiXNS-H}_2\text{O}$  and  $\text{Ni@SiXNS-EtOH}$  samples, respectively. For  $\text{Ni@SiXNS-H}_2\text{O}$ , the exposed Ni on the surface of SiXNS could easily bridge-bond to  $\text{CO}$ , leading to the hydrogenation of  $^*\text{C}$  to  $\text{CH}_4$  following  $\text{CO}$  dissociation. For  $\text{Ni@SiXNS-EtOH}$ , the confined Ni sites are unable to form bridging  $^*\text{CO}$  species and formate species were instead the main intermediates leading to  $\text{CH}_4$  production.

The gradual increase of the  $\text{CH}_4$  production rate on  $\text{Ni@SiXNS-EtOH}$  in Fig. 5d originated from the gradual release of Ni during the  $\text{CO}_2$  methanation reaction, corresponding well with the recent popular catalytic concept of the “sustained release catalyst,” designed to maintain the high reactivity and stability of the obtained catalyst<sup>54,55</sup>. A thorough in-situ Extended X-Ray Absorption Fine Structure (EXAFS) study illustrated the gradual evolution of Ni in  $\text{Ni@SiXNS-EtOH}$  under simulated reaction conditions (Supplementary Fig. 9). Due to the fact that the reaction under light conditions probably resulted in a higher reactor temperature than  $300^\circ\text{C}$ , and that the high flow rate would bring down the surface temperature, we performed the in-situ EXAFS study at  $330^\circ\text{C}$  at a flow of 4:1  $\text{H}_2/\text{CO}_2$  (i.e., 130 s.c.c.m. 3.5%  $\text{H}_2$  in He and 60 s.c.c.m. 2%  $\text{CO}_2$  in He) after  $\text{H}_2$  activation at  $300^\circ\text{C}$ . Significant changes in the XAS spectra began to occur and continued over a 90 min period. The changes continued but gradually

slowed and so the temperature was again increased to  $350^\circ\text{C}$  in order to more rapidly drive the sample toward redox equilibrium, which was reached within the following 90 min period. This matched well with the rapid attainment of a steady  $\text{CH}_4$  or  $\text{CO}$  formation rate in a stability test of  $\text{Ni@SiXNS-EtOH}$  under dark conditions at  $300^\circ\text{C}$  with pre-reduction at  $350^\circ\text{C}$  (Supplementary Fig. 10).

On the origin of high selectivity for  $\text{CH}_4$  production of  $\text{Ni@SiXNS-EtOH}$ , apparent reaction orders were estimated from the variation in production rates with different inlet reactant concentrations according to the rate law equation  $r = kP_{\text{H}_2}^a P_{\text{CO}_2}^b$  (Supplementary Fig. 11, Supplementary Table 1, and Supplementary Notes) after the sample was stabilized, as described above. The apparent reaction orders of  $\text{CO}_2$  and  $\text{H}_2$  were 0.40 and 1.56, respectively, for  $\text{CH}_4$  production, whereas the reaction orders of  $\text{CO}_2$  and  $\text{H}_2$  were 2.80 and 0.28 for  $\text{CO}$  production. Thus, the relatively large reaction order value of  $\text{H}_2$  implies dominant control of the  $\text{CH}_4$  production rate by the partial pressure of  $\text{H}_2$ , which is indicative of the associative methanation pathway in which  $\text{H}_2$  fully hydrogenates the activated  $\text{CO}_2$ . In contrast, for  $\text{CO}$  production, the much larger reaction order of  $\text{CO}_2$  indicates its greater dependence on  $\text{CO}_2$  adsorption and dissociation.

Over the range of  $\text{H}_2$  partial pressure variations explored, it was determined that the fractional yield of  $\text{CH}_4$  from  $\text{CO}_2$  was consistently larger than that for  $\text{CO}$  production from  $\text{CO}_2$ , indicating high selectivity toward  $\text{CH}_4$  production. Further analysis revealed the rate-limiting step to be the decomposition and further hydrogenation of formate-type species  $\text{HCOOH}^*$  (see Supplementary Information).

The crucial finding of this study is that control over the location of the Ni nanoparticles, either at the interior or exterior regions of the SiXNS, matters when it comes to selectivity favoring the methanation vs. the reverse water–gas shift reaction. The  $\text{CO}$  pathway dominates for Ni at the exterior of the nanosheets, whereas the formate pathway is preferred for Ni confined to the interior. Although the former does not discriminate much between  $\text{CO}$  and  $\text{CH}_4$  products, the latter strongly favors  $\text{CH}_4$ . This innovative approach to the construction of designed architecture 2D  $\text{Ni@SiXNS}$  nanocomposites presents a paradigm in the field of gas-phase heterogeneous (photo)catalytic hydrogenation of  $\text{CO}_2$  to synthetic chemicals and fuels.

## Methods

**Synthesis of SiXNS and NiO@SiXNS.** In a typical synthesis of SiXNS, 1.0 g of calcium silicide powder (Fluka™) was dispersed in 100 mL hydrochloric acid (36%, Caledon Laboratory Chemicals) pre-cooled to  $0^\circ\text{C}$  in a jacketed flask with a circulator (NESLAB™ RTE-111). The mixture was stirred under inert atmosphere for 6 days at  $0^\circ\text{C}$ . The solid product was collected via vacuum filtration, washed with anhydrous acetone, and dried under  $\text{N}_2$  flow before being stored under vacuum in a desiccator. For the synthesis of  $\text{NiO@SiXNS-EtOH}$ , 0.0124 g of nickel nitrate hexahydrate (Alfa Aesar) was dissolved into 1 mL of ethanol. Next, 0.048 g of SiXNS was dispersed into 2 mL of ethanol and sonicated for 30 min. Then the nickel nitrate ethanol solution was added into the SiXNS dispersion and sonicated for another 30 min. Next, it was placed at room temperature for 12 h and dried in vacuum at  $70^\circ\text{C}$  for 24 h before being cooled down to room temperature under vacuum for 12 h. The powder sample was finally calcined at  $400^\circ\text{C}$  in air for 3 h. The process for the synthesis of  $\text{NiO@SiXNS-H}_2\text{O}$  was similar to that of  $\text{NiO@SiXNS-EtOH}$ , except that the solution was changed to an equal volume of distilled water.

**Synthesis of control samples.** For  $\text{NiO@SiO}_2$ , 0.0124 g of nickel nitrate hexahydrate (Alfa Aesar) was dissolved into 1 mL of distilled water.  $\text{SiO}_2$  (0.048 g; Aldrich, fumed, powder,  $0.007 \mu\text{m}$ ) was dispersed into 2 mL of distilled water and sonicated for 30 min. The nickel nitrate solution was then added into the  $\text{SiO}_2$  dispersion and sonicated for another 30 min. After that, it was held at room temperature for 12 h and dried in vacuum at  $70^\circ\text{C}$  for 24 h. The powder sample was finally calcined at  $400^\circ\text{C}$  in air for 3 h. The industrial  $\text{Ni@Al}_2\text{O}_3$  catalyst was purchased from Riogen (10 wt% Ni) and used as received.



**Material characterizations.** An ICP-AES (Thermo iCAP 6300 spectrometer) was used to measure the nickel content in the NiO@SiXNS samples. PXRD was performed on a Bruker D2 Phaser X-ray diffractometer, using Cu  $K_{\alpha}$  radiation and an accelerating voltage of 30 kV. Nitrogen adsorption experiments were carried out at 77 K on a Quantachome Autosorb-1-C instrument. Prior to each adsorption measurement, the samples were degassed at 150 °C overnight under vacuum. The specific surface area was determined using the BET equation, applied to the best linear fit within the range of  $0.05 \leq P/P_0 \leq 0.35$ . FTIR was conducted by using a Perkin Elmer Spectrum One FTIR fitted with a universal attenuated total reflectance sampling accessory with a diamond-coated zinc selenide window. Diffuse reflectance of the samples was measured using a Lambda 1050 UV/Vis/NIR spectrometer from Perkin Elmer and an integrating sphere with a diameter of 150 mm. SEM and TEM images were taken on a Hitachi S-5200 high resolution “in lens” scanning electron microscope. EDX mapping was performed using an Oxford Inca EDX system. High-resolution TEM images of the samples were obtained on a FEI Tecnai G<sup>2</sup>-F20 system operated at 200 kV. For the electron tomography analysis, the powder of the Ni@SiXNS sample was dispersed on 100 × 400 mesh carbon-coated copper grids (Quantifoil), where 15 nm colloidal Au particles had been deposited before. Electron tomography was performed using a Fischione 2020 tomography holder on a FEI Titan 80–300 microscope operated at an acceleration voltage of 300 kV in scanning transmission electron microscopy (STEM) mode. High-angle annular dark field (HAADF) STEM tilt-series images were collected using the Xplore3D software (FEI) over the tilt range of  $\pm 76^\circ$  with the increment of  $2^\circ$ . Alignment of the tilt series was performed using IMOD using the Au particles as fiducial markers and achieved a mean residual alignment error of 0.60 pixels. The aligned tilt series was reconstructed using the simultaneous iterative reconstruction algorithm within Inspect3D (FEI). The resultant tomogram had a final voxel size of 3.69 nm. The 3D image analysis and visualization of the reconstruction tomogram was performed in Amira 6.0. XPS was performed in an ultra-high vacuum chamber with base pressure of  $10^{-9}$  Torr. The system used a Thermo Scientific K-Alpha XPS spectrometer. Samples were prepared for XPS analysis by adhering powders to carbon substrates; all peaks were energy-calibrated relative to the C1s peak of adventitious carbon at 284.8 eV and data analysis was carried out using CasaXPS software. The temperature-programmed reduction by H<sub>2</sub> (H<sub>2</sub>-TPR) was measured on a chemisorption apparatus (Micromeritics AutoChem II 2920). In a typical experiment, 0.1 g of sample was pretreated at 300 °C for 1 h in He (30 s.c.c.m.). Afterwards, the system was cooled to 50 °C, followed by heating to 900 °C at a rate of  $10^\circ\text{C min}^{-1}$  in 10% H<sub>2</sub>/He (30 s.c.c.m.), and the thermal conductivity detector (TCD) signal was recorded. The same apparatus was applied to perform H<sub>2</sub> pulse chemisorption. The sample was first reduced at 300 °C for 1 h in 10% H<sub>2</sub>/He (30 s.c.c.m.), followed by cooling down to 35 °C in He (30 s.c.c.m.). A 10% H<sub>2</sub>/He gas composition was injected into the reduced sample at 5 min intervals, according to the pulse method, until saturation adsorption was observed. XAS spectra were recorded at Sector 9-BM of the Advanced Photon Source at Argonne National Laboratory (Lemont, IL). A Quick-EXAFS, double-crystal silicon monochromator was used to obtain time-resolved spectra, with each scan taking <30 s to complete. Gas ionization chambers were used to measure incident and transmitted X-ray intensities, and a Ni foil reference was used for in-line energy calibration of the system. A gas manifold consisting of mass flow controllers and Swagelok compression fittings was used to deliver reactant gases to the sample chamber.

Prior to analysis, a predetermined quantity of each sample was milled together with a boron nitride bulking agent before being pressed into a solid pellet using an aluminum die and pistons. This die, still containing the pressed pellet, was then transferred into a sample chamber equipped with ceramic heating elements (top and bottom), a proportional-integral-derivative (PID) temperature controller, and an outer cooling jacket to prevent the Kapton® windows from being damaged at elevated temperatures. Processing of X-ray absorption near-edge structure (XANES) and EXAFS spectra was performed using Athena, part of the Demeter software package. The reaction chamber was first sealed and purged for several minutes with He gas at a flow rate of 190 s.c.c.m., following which the temperature was increased to 300 °C for reduction in a 190 s.c.c.m. flow of 3.5% H<sub>2</sub> in He.

**Gas-phase CO<sub>2</sub> reduction tests.** Gas-phase photocatalytic reaction was conducted in a plug-flow capillary reactor in accordance with the procedure reported in our previous work<sup>56</sup>. For the catalytic investigation, the sample (~10 mg) was first heated to 300 °C in H<sub>2</sub> (4 s.c.c.m.) and reduced in the dark for 1 h (yielding Ni@SiXNS). Next, a continuous flow of CO<sub>2</sub> and H<sub>2</sub> was introduced with a ratio of 1:4 (1 and 4 s.c.c.m., respectively) controlled by Alicat Scientific digital flow controllers. The catalytic performance of the samples was studied under both dark and light conditions, while being maintained at 300 °C for 30 min for each condition. The amounts of CO and CH<sub>4</sub> produced were determined using online GC with autosampling (GC, Agilent 7820A, HP-PLOT Q PT, 19091P-QO3PT, 15 m<sup>2</sup>.320 mm<sup>2</sup>20 μm) directly connected to the reactor outlet and rates were calculated according to the calibration with standard gases. The stability measurement of the catalyst in photocatalytic reaction was investigated at 300 °C under light irradiation. In order to estimate the apparent reaction orders for CH<sub>4</sub> and CO, the reactivity was stabilized by pre-treating the sample with H<sub>2</sub> at a slightly higher temperature of 350 °C for 1 h and subsequently exposing it to CO<sub>2</sub> and H<sub>2</sub> at 300 °C for 10 h (Supplementary Fig. 10). A stable reactivity was almost reached

within 2 h. In order to further confirm the production of CH<sub>4</sub>, isotopic labeling experiments were performed using <sup>13</sup>CO<sub>2</sub> (99.9 at%, Sigma-Aldrich). Isotope distributions in the product gases were measured using an Agilent 7890A gas chromatograph-mass spectrometer with a 60 m GS-CarbonPLOT column leading to the mass spectrometer. For the rate law equation determination tests and thermal stability tests, CO<sub>2</sub>, H<sub>2</sub>, and Ar were flowed through in various ratios controlled by digital flow controllers (FMA-A2401, OMEGA). The concentration of CO and CH<sub>4</sub> produced were determined using GC-MS (7890B and 5977A, He carrier, Agilent).

**In-situ DRIFT studies.** In-situ DRIFTS experiments were performed on a Thermo Scientific™ Nicolet™ iS50 FT-IR Spectrometer with a mercury cadmium telluride detector cooled with liquid nitrogen. The spectrometer was equipped with a Harrick Praying Mantis™ diffuse reflection accessory and a Harrick high-temperature reaction chamber (HTC) with ZnSe windows. The temperature was controlled by a Harrick ATC-024-3 Temperature Controller. The spectrometer data were obtained using OMNIC software (Thermo Scientific). The autosampling function in the OMNIC software was used to collect data at specific time intervals. The loaded sample in the HTC was pressed carefully to ensure a flat and even surface. The following procedure for data collection was used. The sample was first reduced for 1 h at 300 °C in H<sub>2</sub> (20 s.c.c.m.). Then the background scan was collected under flowing He at the same temperature, such that the spectra collected afterwards were differential spectra. Finally, CO<sub>2</sub>, H<sub>2</sub>, and He were introduced to the sample at a rate of 2, 8, and 10 s.c.c.m. The spectra were collected for 60 min with a resolution of  $4\text{ cm}^{-1}$  and 32 scans.

## Data availability

The authors declare that the main data to support the finds of this study are available within the article and its Supplementary Information. The source data underlying all the plots in the main text and Supplementary Information are provided and available from the corresponding author upon request.

Received: 25 October 2018 Accepted: 7 May 2019

Published online: 13 June 2019

## References

1. Aresta, M., Dibenedetto, A. & Angelini, A. Catalysis for the valorization of exhaust carbon: from CO<sub>2</sub> to chemicals, materials, and fuels. *Technological use of CO<sub>2</sub>*. *Chem. Rev.* **114**, 1709–1742 (2014).
2. Ozin, G. A. Throwing new light on the reduction of CO<sub>2</sub>. *Adv. Mater.* **27**, 1957–1963 (2015).
3. Schlögl, R. The revolution continues: Energiewende 2.0. *Angew. Chem. Int. Ed.* **54**, 4436–4439 (2015).
4. Jelle, A. A. et al. Highly efficient ambient temperature CO<sub>2</sub> photomethanation catalyzed by nanostructured RuO<sub>2</sub> on silicon photonic crystal support. *Adv. Energy Mater.* **8**, 1702277 (2018).
5. Wang, W., Wang, S., Ma, X. & Gong, J. Recent advances in catalytic hydrogenation of carbon dioxide. *Chem. Soc. Rev.* **40**, 3703–3727 (2011).
6. Mills, G. A. & Steffgen, F. W. Catalytic methanation. *Catal. Rev.* **8**, 159–210 (1974).
7. Vogt, C. et al. Unravelling structure sensitivity in CO<sub>2</sub> hydrogenation over nickel. *Nat. Catal.* **1**, 127–134 (2018).
8. Du, G. et al. Methanation of carbon dioxide on Ni-incorporated MCM-41 catalysts: the influence of catalyst pretreatment and study of steady-state reaction. *J. Catal.* **249**, 370–379 (2007).
9. Vita, A. et al. Activity and stability of powder and monolith-coated Ni/GDC catalysts for CO<sub>2</sub> methanation. *Appl. Catal. B Environ.* **226**, 384–395 (2018).
10. Budi, C. S., Wu, H.-C., Chen, C.-S., Saikia, D. & Kao, H.-M. Ni Nanoparticles supported on cage-type mesoporous silica for CO<sub>2</sub> hydrogenation with high CH<sub>4</sub> selectivity. *ChemSusChem* **9**, 2326–2331 (2016).
11. Chen, C.-S., Budi, C. S., Wu, H.-C., Saikia, D. & Kao, H.-M. Size-tunable Ni nanoparticles supported on surface-modified, cage-type mesoporous silica as highly active catalysts for CO<sub>2</sub> hydrogenation. *ACS Catal.* **7**, 8367–8381 (2017).
12. Peebles, D. E., Goodman, D. W. & White, J. M. Methanation of carbon dioxide on nickel(100) and the effects of surface modifiers. *J. Phys. Chem.* **87**, 4378–4387 (1983).
13. Falconer, J. L. & Zaçli, A. E. Adsorption and methanation of carbon dioxide on a nickel/silica catalyst. *J. Catal.* **62**, 280–285 (1980).
14. Heine, C., Lechner, B. A. J., Bluhm, H. & Salmeron, M. Recycling of CO<sub>2</sub>: probing the chemical state of the Ni(111) surface during the methanation reaction with ambient-pressure X-ray photoelectron spectroscopy. *J. Am. Chem. Soc.* **138**, 13246–13252 (2016).
15. Hoffmann, F., Cornelius, M., Morell, J. & Fröba, M. Silica-based mesoporous organic-inorganic hybrid materials. *Angew. Chem. Int. Ed.* **45**, 3216–3251 (2006).

16. Sayari, A. & Hamoudi, S. Periodic mesoporous silica-based organic–inorganic nanocomposite materials. *Chem. Mater.* **13**, 3151–3168 (2001).
17. Liang, J., Liang, Z., Zou, R. & Zhao, Y. Heterogeneous catalysis in zeolites, mesoporous silica, and metal–organic frameworks. *Adv. Mater.* **29**, 1701139 (2017).
18. Potemkin D. I., et al. Porous nanocrystalline silicon supported bimetallic Pd–Au catalysts: preparation, characterization, and direct hydrogen peroxide synthesis. *Front. Chem.* **6**, 85 (2018).
19. Halim, M. Y. A., Tan, W. L., Bakar, N. H. H. A. & Bakar, M. A. Surface characteristics and catalytic activity of copper deposited porous silicon powder. *Materials* **7**, 7737 (2014).
20. Polisski, S. et al. In situ synthesis and catalytic activity in CO oxidation of metal nanoparticles supported on porous nanocrystalline silicon. *J. Catal.* **271**, 59–66 (2010).
21. Polisski, S., Goller, B., Lapkin, A., Fairclough, S. & Kovalev, D. Synthesis and catalytic activity of hybrid metal/silicon nanocomposites. *Phys. Stat. Sol. (RRL)* **2**, 132–134 (2008).
22. Weatherbee, G. D. & Bartholomew, C. H. Hydrogenation of CO<sub>2</sub> on group VIII metals: I. specific activity of NiSiO<sub>2</sub>. *J. Catal.* **68**, 67–76 (1981).
23. Le, T. A., Kim, T. W., Lee, S. H. & Park, E. D. Effects of Na content in Na/Ni/SiO<sub>2</sub> and Na/Ni/CeO<sub>2</sub> catalysts for CO and CO<sub>2</sub> methanation. *Catal. Today* **303**, 159–167 (2018).
24. Guo, M. & Lu, G. The effect of impregnation strategy on structural characters and CO<sub>2</sub> methanation properties over MgO modified Ni/SiO<sub>2</sub> catalysts. *Catal. Commun.* **54**, 55–60 (2014).
25. Sastre, F., Puga, A. V., Liu, L., Corma, A. & García, H. Complete photocatalytic reduction of CO<sub>2</sub> to methane by H<sub>2</sub> under solar light irradiation. *J. Am. Chem. Soc.* **136**, 6798–6801 (2014).
26. Wu, H. C. et al. Methanation of CO<sub>2</sub> and reverse water gas shift reactions on Ni/SiO<sub>2</sub> catalysts: the influence of particle size on selectivity and reaction pathway. *Catal. Sci. Technol.* **5**, 4154–4163 (2015).
27. Li, S. et al. Siloxene nanosheets: a metal-free semiconductor for water splitting. *J. Mater. Chem. A* **4**, 15841–15844 (2016).
28. Badley, R. D. & Johnson, M. M. Siloxene-supported catalysts for ethylene polymerization. *J. Catal.* **141**, 524–532 (1993).
29. Ohashi, M., Yaokawa, R., Takatani, Y. & Nakano, H. Versatile reducing reaction field within layered polysilane for efficient one-pot synthesis of metal nanoparticles. *ChemNanoMat* **3**, 534–537 (2017).
30. Yan, Z., Fu, L., Zuo, X. & Yang, H. Green assembly of stable and uniform silver nanoparticles on 2D silica nanosheets for catalytic reduction of 4-nitrophenol. *Appl. Catal. B: Environ.* **226**, 23–30 (2018).
31. Ono, Y., Sendoda, Y. & Keii, T. Siloxene as a unique catalyst for structural isomerization of butene. *J. Am. Chem. Soc.* **97**, 5284–5285 (1975).
32. Krishnamoorthy, K., Pazhamalai, P. & Kim, S.-J. Two-dimensional siloxene nanosheets: novel high-performance supercapacitor electrode materials. *Energy Environ. Sci.* **11**, 1595–1602 (2018).
33. Nakano H., Ishii M., Nakamura H. Preparation and structure of novel siloxene nanosheets. *Chem. Commun.*, 2945–2947 (2005).
34. Weiss, A., Beil, G. & Meyer, H. The topochemical reaction of CaSi<sub>2</sub> to a two-dimensional subsiliceous acid Si<sub>2</sub>H<sub>3</sub>(OH)<sub>3</sub> (=Kautskys' Siloxene). *Z. Naturforsch.* **34b**, 25–30 (1979).
35. Kautsky, H. & Zocher, H. Über die Beziehung zwischen Chemi- und Photolumineszenz bei ungesättigten Siliziumverbindungen. *Z. für. Phys.* **9**, 267–284 (1922).
36. Fuchs, H. D. et al. Porous silicon and siloxene: vibrational and structural properties. *Phys. Rev. B* **48**, 8172–8189 (1993).
37. Fu, R. et al. Two-dimensional silicon suboxides nanostructures with Si nanodomains confined in amorphous SiO<sub>2</sub> derived from siloxene as high performance anode for Li-ion batteries. *Nano Energy* **39**, 546–553 (2017).
38. Clause, O., Bonneviot, L. & Che, M. Effect of the preparation method on the thermal stability of silica-supported nickel oxide as studied by EXAFS and TPR techniques. *J. Catal.* **138**, 195–205 (1992).
39. Occelli, M. L., Psaras, D., Suib, S. L. & Stencel, J. M. Metal contaminant effects on the properties of a silica-rich fluid cracking catalyst. *Appl. Catal.* **28**, 143–160 (1986).
40. Meng, X. et al. Photothermal conversion of CO<sub>2</sub> into CH<sub>4</sub> with H<sub>2</sub> over group VIII nanocatalysts: an alternative approach for solar fuel production. *Angew. Chem.* **126**, 11662–11666 (2014).
41. Zhang, Z., Vergykios, K. E., MacDonald, S. M. & Affrossman, S. Comparative study of carbon dioxide reforming of methane to synthesis gas over Ni/La<sub>2</sub>O<sub>3</sub> and conventional nickel-based catalysts. *J. Phys. Chem.* **100**, 744–754 (1996).
42. Robbins, J. L. & Marucchi-Soos, E. Evidence for multiple carbon monoxide hydrogenation pathways on platinum alumina. *J. Phys. Chem.* **93**, 2885–2888 (1989).
43. Guo, J., Lou, H., Mo, L. & Zheng, X. The reactivity of surface active carbonaceous species with CO<sub>2</sub> and its role on hydrocarbon conversion reactions. *J. Mol. Catal. A Chem.* **316**, 1–7 (2010).
44. Szanyi, J. & Kwak, J. H. Dissecting the steps of CO<sub>2</sub> reduction: 2. The interaction of CO and CO<sub>2</sub> with Pd/γ-Al<sub>2</sub>O<sub>3</sub>: an in situ FTIR study. *Phys. Chem. Chem. Phys.* **16**, 15126–15138 (2014).
45. Blackmond, D. G. & Ko, E. I. Structural sensitivity of CO adsorption and H<sub>2</sub>CO coadsorption on NiSiO<sub>2</sub> catalysts. *J. Catal.* **96**, 210–221 (1985).
46. Fujita, S.-I., Nakamura, M., Doi, T. & Takezawa, N. Mechanisms of methanation of carbon dioxide and carbon monoxide over nickel/alumina catalysts. *Appl. Catal. A Gen.* **104**, 87–100 (1993).
47. Múnera, J. F. et al. Kinetics and reaction pathway of the CO<sub>2</sub> reforming of methane on Rh supported on lanthanum-based solid. *J. Catal.* **245**, 25–34 (2007).
48. Schubert, M. M., Gasteiger, H. A. & Jürgen Behm, R. Surface formates as side products in the selective CO oxidation on Pt/γ-Al<sub>2</sub>O<sub>3</sub>. *J. Catal.* **172**, 256–258 (1997).
49. Marwood, M., Doepper, R., Prairie, M. & Renken, A. Transient drift spectroscopy for the determination of the surface reaction kinetics of CO<sub>2</sub> methanation. *Chem. Eng. Sci.* **49**, 4801–4809 (1994).
50. Boudjemaa, A. et al. In situ DRIFTS studies of high-temperature water-gas shift reaction on chromium-free iron oxide catalysts. *C. R. Chim.* **14**, 534–538 (2011).
51. Huang, H. et al. Solar-light-driven CO<sub>2</sub> reduction by CH<sub>4</sub> on silica-cluster-modified Ni nanocrystals with a high solar-to-fuel efficiency and excellent durability. *Adv. Energy Mater.* **8**, 1702472 (2018).
52. Kattel, S., Liu, P. & Chen, J. G. Tuning selectivity of CO<sub>2</sub> hydrogenation reactions at the metal/oxide interface. *J. Am. Chem. Soc.* **139**, 9739–9754 (2017).
53. Miao, B., Ma, S. S. K., Wang, X., Su, H. & Chan, S. H. Catalysis mechanisms of CO<sub>2</sub> and CO methanation. *Catal. Sci. Technol.* **6**, 4048–4058 (2016).
54. Qing, S. et al. Strategic use of CuAlO<sub>2</sub> as a sustained release catalyst for production of hydrogen from methanol steam reforming. *Chem. Commun.* **54**, 12242–12245 (2018).
55. Xi, H., Hou, X., Liu, Y., Qing, S. & Gao, Z. Cu–Al spinel oxide as an efficient catalyst for methanol steam reforming. *Angew. Chem. Int. Ed.* **53**, 11886–11889 (2014).
56. Wang, L. et al. Photocatalytic hydrogenation of carbon dioxide with high selectivity to methanol at atmospheric pressure. *Joule* **2**, 1369–1381 (2018).

## Acknowledgements

G.A.O. acknowledges the financial support of the Ontario Ministry of Research and Innovation (MRI), the Ministry of Economic Development, Employment and Infrastructure (MEDI), the Ministry of the Environment and Climate Change's (MOECC) Best in Science (BIS) Award, Ontario Center of Excellence Solutions 2030 Challenge Fund, Ministry of Research Innovation and Science (MRIS) Low Carbon Innovation Fund (LCIF), Imperial Oil, the University of Toronto's Connaught Innovation Fund (CIF), Connaught Global Challenge (CGC) Fund, and the Natural Sciences and Engineering Research Council of Canada (NSERC). X.Y. acknowledge the National Natural Science Foundation of China (Nos. 21878203 and 21406153), Shanxi International Cooperation Project (No. 201703D421037), Shanxi Provincial Key Innovative Research Team in Science and Technology (No. 2014131006), Scientific and Technological Innovation Programs of Higher Education Institutions in Shanxi (No. 2017137), Natural Science Foundation of Shanxi Province (No. 201801D121061), and Program for the Outstanding Innovative Teams of Higher Learning Institutions of Shanxi (154010146-s). We acknowledge Karlsruhe Nano Micro Facility (KNMF) for using the TEM (Proposal 2018-020-023409). P.N.D. gratefully acknowledges financial support from the NSERC PDF program. Beamline scientists Tianpin Wu and George Sterbinsky are acknowledged for their helpful assistance and advice regarding XAS experimental setup and data acquisition. Mireille Ghossoub is acknowledged for her assistance in XAS data acquisition. This research used resources of the Advanced Photon Source, a U.S. Department of Energy (DOE) Office of Science User Facility operated for the DOE Office of Science by Argonne National Laboratory under Contract No. DE-AC02-06CH11357.

## Author contributions

X.Y., W.S. and G.A.O. conceived and designed the experiments. X.Y., W.S., D.L.H.H. and S.G.H.K. prepared the materials for characterization. X.Y., W.S., L. Wan and R.S. carried out the flow experiments for CO<sub>2</sub> methanation. X.Y., W.S. and D.L.H.H. performed the in-situ DRIFTS study. X.Y., W.S., I.G., A.A.J. and J.L. performed SEM and TEM characterization. A.T., Y.L., T.W. and B.D.H. carried out the rate law determination and rate-limiting -step study. W.W., D.W. and C.K. performed the electron tomography analysis. L. Wang performed X-ray photoelectron spectroscopy (XPS) characterization. L.F. ran the H<sub>2</sub>-TPR and chemisorption experiments, and carried out the nitrogen sorption and ICP-AES study. J.G. performed the MS testing using <sup>13</sup>C. P.N.D. performed the XAS experiments. X.Y., W.S., P.N.D. and G.A.O. co-wrote the manuscript. X.Y. and W.S. contributed equally to this work. X.Y. and G.A.O. co-supervised the project. R.L. provided the funding and access to TEM, TPR and nitrogen sorption study. All authors discussed the results and commented on the manuscript.

**Additional information**

**Supplementary Information** accompanies this paper at <https://doi.org/10.1038/s41467-019-10464-x>.

**Competing interests:** The authors declare no competing interests.

**Reprints and permission** information is available online at <http://npg.nature.com/reprintsandpermissions/>

**Journal Peer Review Information:** *Nature Communications* thanks Antonio Vita and the other, anonymous, reviewer(s) for their contribution to the peer review of this work.

**Publisher's note:** Springer Nature remains neutral with regard to jurisdictional claims in published maps and institutional affiliations.



**Open Access** This article is licensed under a Creative Commons Attribution 4.0 International License, which permits use, sharing, adaptation, distribution and reproduction in any medium or format, as long as you give appropriate credit to the original author(s) and the source, provide a link to the Creative Commons license, and indicate if changes were made. The images or other third party material in this article are included in the article's Creative Commons license, unless indicated otherwise in a credit line to the material. If material is not included in the article's Creative Commons license and your intended use is not permitted by statutory regulation or exceeds the permitted use, you will need to obtain permission directly from the copyright holder. To view a copy of this license, visit <http://creativecommons.org/licenses/by/4.0/>.

© The Author(s) 2019